Aberration-free three-dimensional multiphoton imaging of neuronal activity at kHz rates.

Edward J Botcherby, Christopher W Smith, Michael M Kohl, Delphine Débarre, Martin J Booth, Rimas Juskaitis, Ole Paulsen, Tony Wilson

Aberration-free three-dimensional multiphoton imaging of neuronal activity at kHz rates

Edward J. Botcherby[a], Christopher W. Smith[a], Michael M. Kohl[b,c], Delphine Débarre[d,a], Martin J. Booth[a], Rimas Juškaitis[a], Ole Paulsen[b,c], and Tony Wilson[a,1]

[a]Department of Engineering Science, University of Oxford, Parks Road, Oxford OX1 3PJ, United Kingdom; [b]Department of Physiology, Anatomy and Genetics, University of Oxford, Parks Road, Oxford OX1 3PT, United Kingdom; [c]Department of Physiology, Development and Neuroscience, University of Cambridge, Downing Street, Cambridge CB2 3EG, United Kingdom; and [d]Laboratory for Optics and Biosciences, Ecole Polytechnique, 91128 Palaiseau, France

Edited by Jennifer Lippincott-Schwartz, National Institutes of Health, Bethesda, MD, and approved December 19, 2011 (received for review July 26, 2011)

Multiphoton microscopy is a powerful tool in neuroscience, promising to deliver important data on the spatiotemporal activity within individual neurons as well as in networks of neurons. A major limitation of current technologies is the relatively slow scan rates along the *z* direction compared to the kHz rates obtainable in the *x* and *y* directions. Here, we describe a custom-built microscope system based on an architecture that allows kHz scan rates over hundreds of microns in all three dimensions without introducing aberration. We further demonstrate how this high-speed 3D multiphoton imaging system can be used to study neuronal activity at millisecond resolution at the subcellular as well as the population level.

fluorescence microscopy | multiphoton imaging | multiphoton microscopy | three-dimensional microscopy

Neurons process information by integrating many thousands of synaptic inputs arriving at thin processes called dendrites and translating them into action potential output. In order to understand the neural code it is important to study both the activity in dendrites and the action potential outputs of large populations of neurons. However, direct electrical recordings from thin dendrites and simultaneous recordings from multiple identified neurons are difficult to achieve and often not feasible, especially in the in vivo setting. Instead, optical sectioning techniques using two-photon excitation of fluorescent indicators of neuronal activity have established themselves as the method of choice to monitor the activity in thin dendrites and large neuronal populations (1–6). Current technology, however, does not allow the spot of light to be scanned sufficiently fast in all three dimensions to fully address the questions of dendritic integration and neuronal population activity. While it is relatively straightforward to scan the focal spot in the *x-y* plane at kHz rates, scan rates along the *z*-axis are limited to approximately 20 Hz with conventional imaging approaches (7). This is due to the mechanical inertia of the objective lens and specimen during refocusing. Higher-speed refocusing was recently achieved using a carefully designed electrically tunable lens (8), but at the expense of the numerical aperture.

Recently we overcame these fundamental problems and showed that neither speed nor numerical aperture needs to be compromised if we use a different microscope architecture (9). Using this method, the spot can now be scanned along the *z* axis at high speed while still maintaining diffraction-limited performance. In our design, scanning is carried out by moving a lightweight mirror instead of the objective and high-speed axial scanning is achieved without introducing significant spherical aberration. To demonstrate the practical feasibility of this principle, we have implemented our unique scan approach in a custom-built two-photon microscope. With it, we monitored calcium transients both along the dendritic arbor of individual pyramidal neurons and in a population of bulk-loaded neurons from a large volume of brain tissue (10). We are able to show functional responses measured without aberration from different neurons separated by more than 60 μm in depth with a time resolution of 1 ms.

Results

Remote Scanning Two-Photon Microscope. The two-photon microscope designed for these experiments is shown in Fig. 1*A*. The microscope has a lateral scan unit (LSU) to scan the focal spot in the *x-y* plane and an axial scan unit (ASU) to independently scan the focal spot in the *z* direction. Unlike traditional systems, which are only capable of high-speed scanning in the *x-y* plane, this microscope can scan the focal spot along any three-dimensional trajectory at high speed. Both the objective lens L_2 and the specimen remain stationary during imaging because the scanning process is carried out remotely using elements upstream of the objective.

The LSU comprises a pair of orthogonally mounted galvanometer mirrors spaced closely together so they can be considered to lie in a single plane. This plane is optically conjugated to the entrance aperture of the ASU using standard optics. Plane waves entering the LSU are thereby imaged onto the entrance aperture of the ASU with an angle that depends on the orientation of the galvanometer mirrors. The ASU, which comprises a lens and a mirror, can be set to retro-reflect light entering it by placing the mirror in the focal plane of the lens. In this configuration, plane waves reemerge from the ASU through the entrance aperture and are further imaged into the pupil plane of L_2, once again using standard optics. In terms of optical rays passing through the system, this arrangement sets up a bundle of parallel rays that enter the pupil of L_2. As this objective lens is designed according to the sine condition (11), all these parallel rays converge to a single point in the specimen. By altering the orientation of the galvanometer mirrors in the LSU it is possible to change the angle of the rays passing into L_2 and consequently the focal spot is displaced laterally. Due to the sine condition, the rays still converge to a single point and diffraction-limited performance is maintained.

The drawback with using sine-condition lenses, however, is that it can be very hard to scan the spot in the axial direction without distorting its shape. For instance, if we try to use a simple quadratic converging or diverging wavefront to refocus the spot, rays entering the pupil at its periphery would focus to a different point along the axis to the rays entering the pupil at the center. The focal spot therefore becomes less confined, has lower peak

Author contributions: E.J.B., C.W.S., M.M.K., D.D., M.J.B., R.J., O.P., and T.W. designed research; E.J.B., C.W.S., and M.M.K. performed research; E.J.B., C.W.S., and M.M.K. analyzed data; and E.J.B., C.W.S., M.M.K., R.J., O.P., and T.W. wrote the paper.

The authors declare no conflict of interest.

This article is a PNAS Direct Submission.

Freely available online through the PNAS open access option.

[1]To whom correspondence should be addressed. E-mail: tony.wilson@eng.ox.ac.uk.

This article contains supporting information online at www.pnas.org/lookup/suppl/doi:10.1073/pnas.1111662109/-/DCSupplemental.

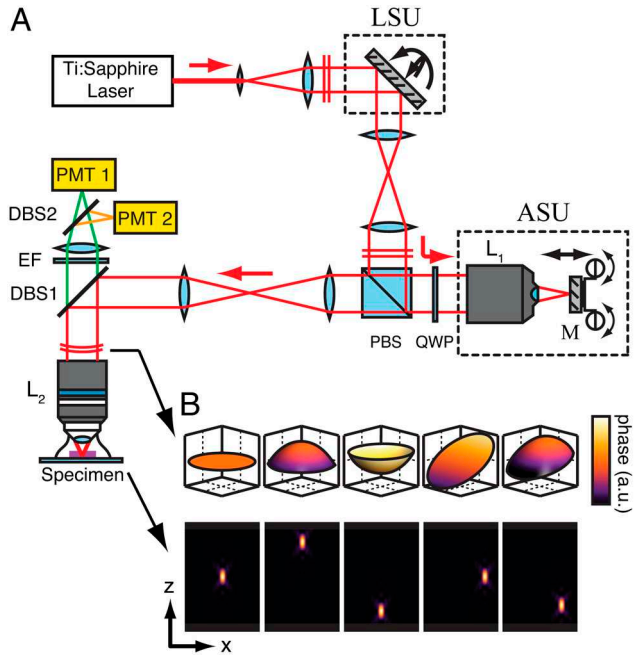

Fig. 1. (*A*) Schematic of the fast focusing two-photon imaging system. *x-y* scanning was carried out by two galvanometers in the lateral scan unit (LSU) and *z*-scanning by the mirror *M* in the axial scan unit (ASU). A polarizing beam splitter (PBS) and quarter-wave plate (QWP) directed all light through the ASU and into the imaging objective (L_2). (*B*) Theoretical wavefronts and intensity distributions produced for various settings of the LSU and ASU. In the central position, where mirror *M* lies in the focal plane of L_1, the resulting wavefront is flat. For positive and negative displacements of the mirror, curved wavefronts are produced and the spot refocuses along the axis. The effect of the LSU is to tilt the wavefronts, which displaces the spot laterally in the specimen and the combination of both ASU and LSU together can shift the spot to any 3-dimensional location in the specimen.

intensity, and is no longer diffraction-limited. This effect, known as spherical aberration (12), significantly reduces resolution and signal-to-noise ratio.

This is not to say that objective lenses cannot produce a diffraction-limited focal spot at a different position along the axis—they can. They just need a beam with a very specific wavefront profile. In this system we generate this specific wavefront profile in the ASU using a second objective lens L_1 to mimic the optical properties of L_2. Crucially, this second objective also obeys the sine condition. If the mirror M is displaced axially from the focal plane, a wavefront emerges from the ASU with the exact profile required for L_2 to produce a single diffraction-limited spot displaced along the axis in the specimen. All that is needed then is to reimage this wavefront profile into the pupil of L_2, which is done here with standard optics. In other words, L_1 modifies the wavefront with equal and opposite aberrations in anticipation of those that L_2 will introduce when focusing away from the focal plane. Fig. 2 shows how the rays are focused by the imaging objective L_2 for two different settings of the mirror M. In these cases the rays striking the pupil are no longer parallel but still converge to a single point.

We now explore this effect further by considering the wavefront of the beam rather than its ray constituents. To produce a diffraction-limited spot of light a distance z from the nominal focal plane, the mathematical expression for the wavefront required in the pupil of L_2 is given by (13):

$$\Delta\Psi_{\text{obj}}(\rho_2,z) = kNA_2 z\sqrt{\text{cosec}^2\alpha_2 - \rho_2^2}, \qquad [1]$$

where $k = 2\pi/\lambda$ is the wavenumber and NA_2, α_2 and ρ_2 are respectively the numerical aperture, angular aperture, and normalized pupil radius of L_2. If a low-NA lens were used in the ASU then moving the mirror would produce either a converging or diverging wavefront with a simple quadratic profile that does not fit this requirement exactly. The resulting wavefront error would contain higher-order polynomial terms that can be interpreted as corresponding to spherical aberration (12). By "mimicking" the optics of the imaging objective, however, the ASU produces a wavefront that is very similar in form:

$$\Delta\Psi_{\text{ASU}}(\rho_1,z) = kNA_1 \cdot 2z_M\sqrt{\text{cosec}^2\alpha_1 - \rho_1^2}, \qquad [2]$$

where z_M is the displacement of the mirror M from the focal plane of L_1 and NA_1, α_1, and ρ_1 are respectively the numerical aperture, the angular aperture, and the normalized pupil radius of L_1. The extra factor of 2 in this equation comes from the reflection geometry: for any displacement of the mirror M the optical path between lens and mirror is increased or decreased by twice that displacement. With a simple magnification this can be transformed into the exact wavefront required by L_2 for diffraction-limited refocusing. In practice, this magnification is provided by the 4f system linking the pupils of L_1 and L_2. Using a magnification factor that asserts $\frac{\rho_2}{\rho_1} = \frac{\sin\alpha_1}{\sin\alpha_2}$, the wavefront generated in the pupil of L_2 becomes:

$$\Delta\Psi(\rho_2,z) = kNA_2 \cdot 2z_M\frac{n_1}{n_2}\sqrt{\text{cosec}^2\alpha_2 - \rho_2^2}, \qquad [3]$$

where n_1 and n_2 are the refractive indices of the immersion media for L_1 and L_2 respectively.

Comparing this expression with Eq. **1**, we see that this specific situation produces a diffraction-limited focal spot a distance $z = 2z_M n_1/n_2$ from the nominal focal plane in the specimen. By varying z_m, the position of the mirror, the focal spot is proportionally displaced to a different axial position in the specimen.

The simplest system that could be built on this principle would have identical lenses for L_1 and L_2. Strictly speaking, perfect compensation of aberrations only happens when focusing into a medium of uniform refractive index so it is desirable to use a water-immersion lens for L_2 as this leads to the best match of refractive index when imaging biological tissues. On the other hand, it is desirable to use a dry lens for L_1 as viscous forces from an immersion medium would otherwise impede the motion of the mirror. This is not a problem as nonidentical lenses may be used so long as the magnification between them is chosen correctly. For this, it is necessary to calculate the normalized pupil radius for each lens using $\rho = rfNA$, where r is the physical radius in the objective pupil and f is the focal distance, which in turn is related to the nominal tube length, F, and magnification of the objective, M, by $f = \frac{F}{M}$. In our system we used an Olympus UApo/340, 40X, 0.9 NA dry objective for L_1 and an Olympus LUMPlanFL N 40X

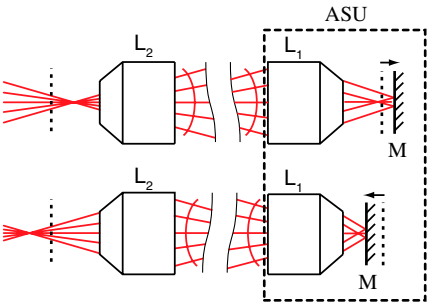

Fig. 2. Ray diagrams showing the ray paths in the focal regions of L_1 and L_2 for two different focal settings. In each case all rays focus through a single point in the specimen irrespective of the focal setting.

0.8 NA water dipping lens for L_2 so the magnification between L_1 and L_2 required for aberration-free imaging was $\frac{r_2}{r_1} = \frac{n_2}{n_1} = 1.33$.

Fig. 1 *B* shows the theoretical wavefronts and corresponding focal spot intensity distributions in the *x-z* plane generated for a series of different LSU and ASU settings. As can be seen in the final pair of plots, we can use the LSU and ASU together to move the focal spot to an arbitrary position in three-dimensional space, away from both the focal plane and the optical axis.

As a result of employing this remote scanning technique, the peak intensity of the focal spot, image resolution, and sectioning strength are all maintained even when imaging at substantial distances from the nominal focal plane of the microscope objective lens. To scan the lightweight mirror *M* at high speed a custom-built actuator was constructed using a pair of galvanometer motors (Fig. 3 *A*). This arrangement permitted a flat frequency response up to 2.7 kHz (Fig. 3 *B*). Further details concerning the construction of the actuator are given in the *Methods* section.

Using a previously developed method (13) to measure the focal spot intensity distribution we found the spot could be scanned more than 200 μm in the *z* direction without significant degradation (Fig. 4). The peak intensity in each case was greater than 85% of that measured in the nominal focal plane across the whole 200 μm range. As a final point, these measurements show that the system resolution is still set by the imaging properties of the imaging objective L_2 and that the ASU does not adversely affect it to any great extent.

Arbitrary Line Scanning. Neuronal processes extend over many hundreds of microns in three dimensions so to monitor activity in these processes, or over a large number of neuronal cell bodies, it is desirable to scan the focal spot over large distances to record activity from different locations with a high temporal resolution. To test the performance of our system we defined a series of complex trajectories through which we scanned the focal spot and observed how faithfully these trajectories were reproduced at different scan frequencies.

For each trajectory a set of points was defined in three-dimensional space. Periodic cubic splines were then fitted through these to define a scan trajectory and galvanometer drive signals were calculated for each scan axis. Due to the nonperfect frequency response characteristics of the galvanometers these signals had to be modified using a precompensation algorithm; otherwise the focal spot would follow a distorted trajectory and potentially miss the points of interest completely. The algorithm made use of the galvanometers' optical feedback signals and computed phase and amplitude corrections that were applied to the driving waveforms (see *Supporting Information*). The focal spot could thus be scanned at high frequency with far greater accuracy through the desired points. Three example trajectories are shown in Fig. 5 with and without precompensation. Each spans more than 100 μm in the *z* direction, and corrected trajectories are accurate to within 0.5 μm of each control point. As the complexity of the trajectories increase, the maximum achievable scan rate decreases because of the galvanometer torque limit.

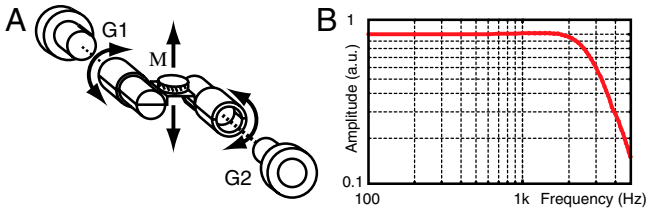

Fig. 3. (*A*) Custom-built actuator for scanning the mirror *M* in the ASU. The mirror *M* is mounted on a flexible beryllium copper bridge and two further galvanometers, G1 and G2, rotate synchronously to produce axial motion. (*B*) The experimentally measured frequency response curve for this actuator when scanning the focal spot 25 μm along *z* direction in the specimen.

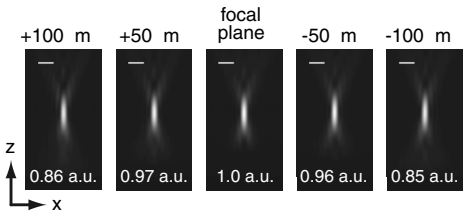

Fig. 4. Non-normalized experimental measurements of the focal spot intensity distribution in the *x-z* plane for different focal settings of the microscope with corresponding peak intensities labeled in arbitrary units. Scale bar 2 μm.

Three-Dimensional Imaging of Neuronal Activity. To validate this technology we considered two classes of problems in neural imaging. We looked first at the activity of a single cell by scanning different dendritic processes. The second case looked at multiple neurons distributed widely in three dimensions in a tissue specimen, scanning at high speed along a cyclic trajectory that passed through the soma of each cell. We demonstrate that the system can be used to scan along the dendritic arbor of individually Fluo-4 dye-loaded neurons to follow dendritic calcium signals in real time and sample the activity of a large number of neurons in an OGB1-AM bulk-loaded sample (see *Methods*).

To test the ability of this remote scanning microscope to provide fast, multisite measurements of dendritic activity, we monitored localized calcium transients in response to backpropagating action potentials that were triggered by current injection through the somatic patch pipette. In order to simulate experiments carried out in vivo, we obtained whole-cell patches from neurons in a cortical slab (Fig. 6*A*). Neurons, about 200–300 μm below the cortical surface, were filled with the calcium-sensitive fluorescent dye Fluo-4 and the fluorescent structural dye Alexa 594 to visualize the fine structure of neuronal processes. Dendritic activity could then be monitored by measuring relative intensity changes (ΔF/F) over time. The remote scanning method was used to obtain a stack of images of the neuron allowing a three-dimensional structural reconstruction (Fig. 6 *B* and *C*). This reconstruction was then used to select points for functional imaging on two dendrites separated by at least 30 μm in depth (Fig. 6*D*).

In addition to single-cell investigations, our system can also measure the behavior of multiple neurons in a cluster. Neurons in the somatosensory cortex were bolus-loaded with a calcium dye OGB1-AM. As before, a three-dimensional reconstruction of the loaded neurons was used to mark neurons in the stack for functional imaging (Fig. 6 *E* and *F*). Extracellular electrical burst stimulation resulted in calcium transients in all neurons that were

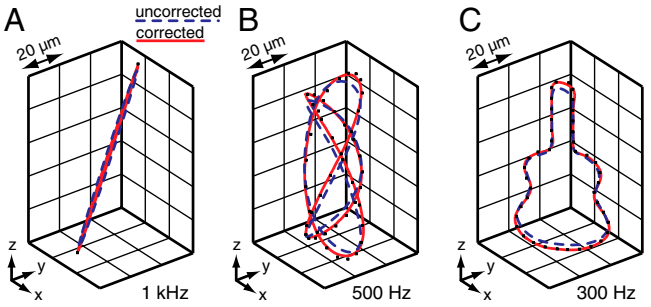

Fig. 5. Experimental verification of arbitrary line scanning. Black squares mark points of interest through which it is desired to scan the focal spot. A continuous trajectory is defined by fitting periodic cubic splines through these and a correction algorithm is applied to compensate for the response characteristics of the galvanometers. Dashed blue and solid red lines indicate respectively the trajectory followed before and after correction. (*A*) Scanning two points at a sampling rate of 1 kHz. (*B*) Scanning points on a three-dimensional Lissajous figure with a sampling rate of 500 Hz. (*C*) Scanning points on a complex arbitrary trajectory at 300 Hz. After correction, the focal spot passes within 0.5 μm of each desired point in all three trajectories.

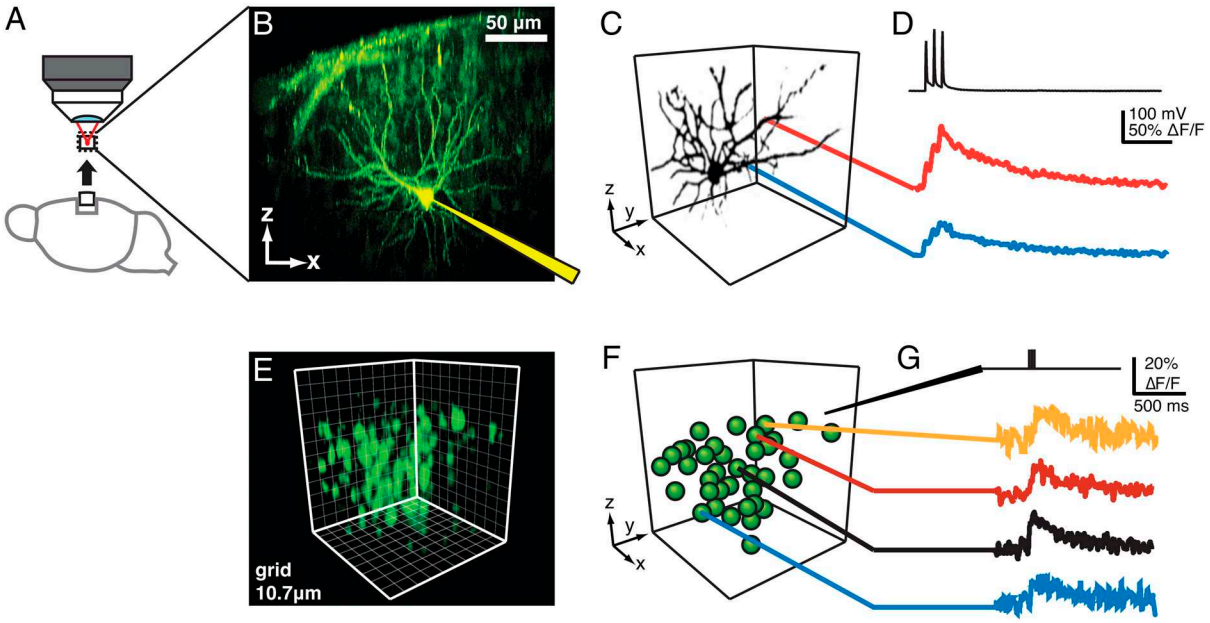

Fig. 6. Functional imaging of cortical neurons. (*A*) Imaging was performed in cortical slabs to emulate the use of this method in the in vivo setting. (*B*) Projection of three-dimensional image stack in *x-z* plane showing a single cell loaded with Fluo-4 and Alexa 594. (*C*) Three-dimensional rendering of a single cell with two points marked that are separated by more than 30 μm in the *z* direction. (*D*) Fluorescence measurements from points of interest taken with a temporal resolution of 500 Hz. (*E*) Three-dimensional rendering of neuronal population bolus-loaded with OGB1-AM. (*F*) Three-dimensional representation of the neurons in the scanned volume ($100 \times 100 \times 100$ μm). (*G*) Fluorescence measurements from different points in the stack in response to extracellular electrical burst stimulation taken with a temporal resolution of 1 kHz and over more than 60 μm *z* distance. Traces represent the average of 2–4 trials.

monitored over a depth of more than 60 μm at 1 kHz acquisition rate (Fig. 6*G*).

Discussion

We have built a two-photon microscope that can be used to image neuronal activity in three dimensions with a high sampling rate. This is achieved by the use of a fundamentally new optical approach, the ASU, which allows an aberration-free focal spot to be repositioned axially at high speed. Compared with previous inertial-based scanning systems, which permit absolute maximum scan speeds of 20 Hz in the *z* direction (7), we have demonstrated that rates of up to 2.7 kHz are achievable with our system. This is comparable with galvanometer scan rates in the *x-y* plane and we believe further development of this technology will eventually allow all axes to be scanned at the same rate.

Reddy et al. (14) have developed an interesting alternative to this approach which uses noninertial scanning, whereby a combination of four acousto-optic deflectors (AODs) are used to generate wavefront profiles so as to position the focal spot arbitrarily in three dimensions. The attractive feature of this approach is that, aside from a short transition time on the order of microseconds, the focal spot can be translated an arbitrary distance in the specimen without passing through any intermediate points. This is not possible with galvanometer-based scanners as the response characteristics essentially prohibit the spot from being repositioned instantaneously so instead a continuous trajectory must be scanned through the points of interest. The drawback of AOD scanning, however, is that a certain amount of spatial and temporal dispersion is introduced by the AODs themselves, and while these effects can be compensated for, this adds to the complexity of system design (15, 16). Kirkby et al. have refined this approach considerably and have achieved a scan range of 137 μm in the *z* direction (17). Nonetheless, aberrations remain and we therefore suggest a useful compromise would be to combine these techniques in a hybrid arrangement that performs *x-y* positioning with AODs and *z* scanning using the ASU approach described in this paper. In this way, we would be able to address random points while scanning quickly over a large range in the *z* direction, without introducing aberrations.

The approach taken here is not limited to applications in neuroscience and will also prove useful for imaging tasks where it is absolutely necessary that the specimen remains stationary and undisturbed and/or where high scan speeds along the *z* direction are of importance. This includes the possibility for scanning other trajectories such as planes with arbitrary orientation (18, 19) or even along curved surfaces at high speed. As a final point we also note that this architecture lends itself to parallelization for situations where multiple points must be imaged simultaneously (20).

In summary, the system we have developed will provide neuroscientists with the tools necessary to study neuronal activity at the population and subcellular levels over large enough distances and at a speed that allows the activity of single action potentials to be followed. This will enable us to study synaptic integration and the neuronal population activity at an unprecedented level of detail. Our remote scanning technology also prevents motion artifacts from being introduced by the mechanical agitation of the tissue as a result of moving the objective lens directly. Furthermore, we have demonstrated in cortical slabs that high-speed *z* scanning with near diffraction-limited resolution is possible allowing for detailed reconstructions and functional imaging in three dimensions, making this technique ideal for in vivo applications (21). We therefore believe this technique presents an important improvement of existing two-photon scanning methods and will significantly facilitate the study of neuronal integration and population activity.

Methods

Two-Photon Imaging. We custom-built a two-photon imaging system around an Olympus BX60M upright microscope stand using mechanical components from the Linos microbench range. A two-dimensional *x-y* stage (Luigs & Neumann) was fitted to the optical bench on which the specimen and patch-clamp head stage could be mounted. The laser source used was a Ti:Sapphire laser (Tsunami, Spectra Physics), producing ultrafast pulses with central wavelength 850 nm ($\Delta\lambda \sim 50$ nm, pulse length approximately 100 fs). Initially, this was expanded to form a plane wave with Gaussian width 5 mm and directed into the lateral scan unit (LSU), comprising two orthogonally mounted

galvanometer mirrors (VM1000+, Cambridge Technology) that controlled the angular orientation of the wavefronts. From here the wavefronts were imaged into the pupil of L_1 using a 4*f* imaging system comprising two achromatic doublet lenses, with focal lengths 120 mm and 160 mm, to produce a magnification of 4/3. L_1 was an Olympus UApo/340, 40X, 0.9 NA dry objective, chosen for its favorable transmission characteristics at 850 nm. As this objective lens is coverslip-corrected a standard 170 μm glass coverslip was fixed to the front for optimal performance. Light passing through L_1 reflected off the mirror M (PF03-03-P01, Thor labs) and passed back through the lens. The emerging wavefront was then reimaged into the pupil plane of L_2 using a further 4*f* system of achromatic doublets, this time with focal lengths 150 mm and 200 mm, to produce a magnification of 4/3. All experiments were performed using an Olympus LUMPlanFL N 40X 0.8*NA* water dipping objective for L_2. A polarizing beam splitter (PBS) and quarter-wave plate (QWP) ensured all light entering the ASU was transmitted into the final stage of the system. A dichroic beamsplitter (DBS) (720DCSPXR, Chroma) and emission filter (EF) (ET720SP-2P8, Chroma) were used to separate fluorescence photons produced in the specimen in the range 400–720 nm for measurement on the photomultiplier tube (PMT) (P30PC-54, Sens-Tech). System scanning and photon counting were carried out with a reconfigurable I/O card (NI PCI-7830R, National instruments), which also produced digital pulses for stimulating action potentials in patch-clamp experiments. Software to control the microscope and interface with a desktop PC was written in Labview (National Instruments).

Construction of Fast Moving Mirror. To provide the stroke and bandwidth required for high-speed refocusing we developed a unique actuator (Fig. 3 *A*) for scanning the mirror *M*. This comprised two galvanometer motors, G1 and G2 (VM1000+, GSI), mounted in opposite directions with their axes parallel and offset by 10 mm. Two custom-made aluminum clamps were attached to the ends of the galvanometer shafts that gripped the ends of a thin strip of beryllium copper, of thickness 100 μm, folded to produce a flexible raised platform between the galvanometers on which the mirror was glued. In operation the galvanometers rotated synchronously, giving the mirror a smooth and repeatable motion. We measured the frequency response (Fig. 3 *B*) of this actuator up to 5 kHz, while scanning the focal spot 25 μm axially in the specimen, using optical feedback signals from both galvanometers. This indicates a bandwidth of 2.7 kHz.

Determining the Mirror Damage Threshold. As the mirror M (Figs. 1 *A* and 2) lies in the focal region of L_1, it is routinely exposed to high peak intensities during imaging, particularly when in focus. We therefore carried out a study to find a mirror with a high damage threshold suitable for use in our system. A number of mirrors were tested by placing them in the focal region of L_1 and exposing them to the full power of the laser beam. The mirrors were also scanned in a slow sinusoidal fashion along the axis ($\Delta z \sim 20$ μm, rate approximately 10 Hz) to ensure worst-case conditions in terms of intensity were invoked at some point in the cycle. One mirror from Thorlabs (PF03-03-P01) was found to be particularly suitable for our system, showing no signs of damage after a prolonged exposure of 1 h under these conditions. During this time the average Ti:Sapphire laser power (pulses approximately 100 fs) entering the back aperture of imaging lens L_2 was found to be 120 mW.

Calibrating the Line Scans. At the beginning of each experiment a through focus series of images was acquired from the specimen volume and *x-y*, *y-z*, and *x-z* image projections displayed on a computer using custom-software. On these projections, points of interest could be marked at arbitrary locations in three dimensions through which it was desired to scan the focal spot. A continuous scan trajectory was then generated using periodic cubic spline functions using these points of interest as nodes. A calibration algorithm was then run to correct for amplitude and phase distortions introduced by the galvanometer scanners so as to ensure that the focal spot would be driven through these points of interest. This involved pixelating the continuous trajectory into a series of discrete points that were equally spaced in three dimensions and calculating a series of command voltages for each of the *x-*, *y-*, and *z-* axes. The number of pixels as well as a pixel dwell time could be selected on the software. Calibration then proceeded for each galvanometer in turn. The command signal was sent to the galvanometer and a feedback signal recorded. This was cross-correlated with the command signal and a best-fit phase lag, $\Delta\Phi$, was determined for the axis (Fig. S1). The reverse of this lag was then applied to the whole command signal to generate a phase-corrected command signal. The galvanometer was then driven afresh using this and a phase-corrected feedback recorded. Deviations, ΔV_i, of the phase-corrected feedback from the initial command signal were calculated at the scan pixels corresponding to each point of interest (Fig. S2), and by correcting each node with ΔV_i and refitting the splines, an amplitude-and-phase-corrected command signal was generated. By iterating this procedure a number of times it was possible to generate a trajectory that passed far closer to the desired points of interest (Fig. S3). This process was repeated for all three galvanometer axes.

Tissue Preparation. Cortical slabs and thalamocortical slices (350 μm thick) were prepared from postnatal day 13–28 C57BL/6 mice of both sexes after decapitation under deep isoflurane-induced anesthesia, in accordance with British Home Office regulations. Slabs were *ca.* 5 × 5 mm and 3 mm deep and cut from the cortical surface in the region of the somatosensory cortex. To anchor the slabs and slices were anchored by mounting them on cover slips (coated with 0.1% poly-L-lysine in ultrapure H_2O). The mounted slices were kept at room temperature (20–25 °C) in small round petri dishes between humidified carbogen gas (95% O_2, 5% CO_2) and artificial CSF (aCSF, containing (in mM): 126 NaCl, 3 KCl, 1.25 NaH_2PO_4, 2 $MgSO_4$, 2 $CaCl_2$, 26 $NaHCO_3$, and 10 glucose, pH 7.2–7.4) for at least 1 h for recovery and then until used for recording. For recordings, the coverslip with slice was transferred to a submerged style recording chamber, and superfused with aCSF, bubbled with carbogen gas.

Electrical and Optical Measurements. Whole-cell patch-clamp recordings were performed with glass pipettes, pulled from standard borosilicate glass (5–8 MOhm). Signals were acquired at 5 kHz and low-pass filtered at 2 kHz using an Axon Multiclamp 700B amplifier (Molecular Devices). Pipette solution contained (in mM): 110 potassium-gluconate, 40 Hepes, 2 ATP-Mg, 0.3 GTP, and 4 NaCl (pH 7.2–7.3; osmolarity 270–285 mosmol l^{-1}) and a combination of a structural label, 40 μM Alexa 594, and a calcium-sensitive dye, 200 μM Fluo-4 (both Molecular Probes). Neurons in the somatosensory cortex were patched using infrared differential-interference contrast imaging (22) at depths approximately 200–300 μm below the surface of the cortical slab and 100–150 μm below the surface of the slice, respectively. Calcium imaging was begun about 30 min after establishing whole-cell configuration, to allow for dye wash-in and diffusional equilibration. Cell populations were labeled with the calcium indicator Oregon Green BAPTA-1 (Molecular Probes) using the multicell bolus loading technique (3, 23). Briefly, 50 μg of the membrane-permeant acetoxymethyl (AM) ester form of OGB-1 was dissolved in DMSO plus 20% Pluronic F-127 (Molecular Probes) and diluted in aCSF to a final concentration of about 1 mM. This solution was pressure-ejected into neocortical layer 2/3 in somatosensory cortex using a micropipette. A tungsten electrode was used to deliver extracellular stimulation bursts.

Data Analysis. Somatic fluorescence signals were analyzed using custom-written scripts in MATLAB (MathWorks) and are expressed as relative fluorescence changes ($\Delta F/F$). Fluorescent signals are presented as averages from 2–4 consecutive trials and smoothed digitally using a 50 Hz low-pass Butterworth filter. Structural renderings were made using Volocity (Perkin Elmer).

ACKNOWLEDGMENTS. This work was supported by the Engineering and Physical Sciences Research Council (EPSCR) (EP/H018565/1), the Biotechnology and Biological Sciences Research Council, and the Wellcome Trust. E.J.B. held an EPSRC postdoctoral research fellowship (EP/F042647/1) and M.M.K. was supported by a Wellcome Trust Prize PhD Studentship.

1. Denk W, Strickler JH, Webb WW (1990) Two-photon laser scanning fluorescence microscopy. *Science* 248:73–76.
2. Svoboda K, Denk W, Kleinfeld D, Tank DW (1997) In vivo dendritic calcium dynamics in neocortical pyramidal neurons. *Nature* 385:161–165.
3. Stosiek C, Garaschuk O, Holthoff K, Konnerth A (2003) In vivo two-photon calcium imaging of neuronal networks. *Proc Natl Acad Sci USA* 100:7319–7324.
4. Helmchen F, Denk W (2005) Deep tissue two-photon microscopy. *Nat Methods* 2:932–940.
5. Svoboda K, Yasuda R (2006) Principles of two-photon excitation microscopy and its applications to neuroscience. *Neuron* 50:823–839.
6. Göbel W, Kampa BM, Helmchen F (2007) Imaging cellular network dynamics in three dimensions using fast 3D laser scanning. *Nat Methods* 4:73–79.
7. Göbel W, Helmchen F (2007) New angles on neuronal dendrites in vivo. *J Neurophysiol* 98:3770–3779.
8. Grewe BF, Voigt FF, van't Hoff M, Helmchen F (2011) Fast two-layer two-photon imaging of neuronal cell populations using an electrically tunable lens. *Biomed Opt Express* 2:2035–2046.
9. Botcherby EJ, Juškaitis R, Booth MJ, Wilson T (2007) Aberration-free optical refocusing in high numerical aperture microscopy. *Opt Lett* 32:2007–2009.
10. Yuste R, Konnerth A (2005) *Imaging in neuroscience and development. A laboratory manual* (Cold Spring Harbor Laboratory Press, Cold Spring Harbor, New York).

11. Born M, Wolf E (1999) *Principles of optics: Electromagnetic theory of propagation, interference and diffraction of light* (Cambridge University Press, Cambridge, UK), (7th edition).
12. Gross H, Zügge H, Peschka M, Blechinger F (2007) *Handbook of Optical Systems, Volume 3, Aberration Theory and Correction of Optical Systems (Fig 33–15)* (Wiley VCH, Weinhein, Germany).
13. Botcherby EJ, Juškaitis R, Booth MJ, Wilson T (2008) An optical technique for remote focusing in microscopy. *Opt Commun* 281:880–887.
14. Reddy GD, Kelleher K, Fink R, Saggau P (2008) Three-dimensional random access multiphoton microscopy for functional imaging of neuronal activity. *Nat Neurosci* 11:713–720.
15. Grewe BF, Langer D, Kasper H, Kampa BM, Helmchen F (2010) High-speed in vivo calcium imaging reveals neuronal network activity with near-millisecond precision. *Nat Methods* 7:399–405.
16. Saggau P (2006) New methods and uses for fast optical scanning. *Curr Opin Neurobiol* 16:543–550.
17. Kirkby PA, Naga Srinivas Nadella KM, Silver RA (2010) A compact acousto-optic lens for 2D and 3D femtosecond based 2-photon microscopy. *Opt Express* 18:13720–13744.
18. Smith CW, Botcherby EJ, Booth MJ, Juškaitis R, Wilson T (2011) Agitation-free multi-photon microscopy of oblique planes. *Opt Lett* 36:663–665.
19. Smith CW, Botcherby EJ, Wilson T (2011) Resolution of oblique-plane images in sectioning microscopy. *Opt Express* 19:2662–2669.
20. Hoover EE, et al. (2010) Remote focusing for programmable multi-layer differential multiphoton microscopy. *Biomed Opt Express* 2:113–122.
21. Grewe BF, Helmchen F (2009) Optical probing of neuronal ensemble activity. *Curr Opin Neurobiol* 19:520–529.
22. Dodt HU, Zieglgänsberger W (1990) Visualizing unstained neurons in living brain slices by infrared DIC-videomicroscopy. *Brain Res* 537:333–336.
23. Garaschuk O, Milos RI, Konnerth A (2006) Targeted bulk-loading of fluorescent indicators for two-photon brain imaging in vivo. *Nat Protoc* 1:380–386.